Available online at www.sciencedirect.com

ScienceDirect

Underground Space 4 (2019) 310–327

www.elsevier.com/locate/undsp

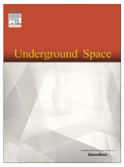

Three-dimensional numerical analysis of the interaction of two crossing tunnels in soft clay

Jin Yin-Fu [a], Zhu Bing-Qing [b], Yin Zhen-Yu [a,*], Zhang Dong-Mei [c,d]

[a] *Department of Civil and Environmental Engineering, The Hong Kong Polytechnic University, Hung Hom, Kowloon, Hong Kong, China*
[b] *China Development Bank Sichuan Branch, No.120, Tiantai Road, Gaoxin District, Chengdu, Sichuan Province, China*
[c] *Key Laboratory of Geotechnical and Underground Engineering of Ministry of Education, Tongji University, Shanghai 200092, China*
[d] *Department of Geotechnical Engineering, Tongji University, Shanghai 200092, China*

Received 1 May 2018; accepted 2 April 2019
Available online 13 May 2019

Abstract

Recently, with the development of underground construction, multi-tunnel engineering has become a matter of concern since the interaction between tunnels at close ranges could cause additional deformation in strata as well as surrounding structures and even serious damage to surface buildings. These tunnel displacement and soil deformation problems can be effectively predicted using numerical methods considering the influence of various factors, such as the anisotropic nature of soft clay. To this end, the anisotropic elastoplastic constitutive S-CLAY1 is implemented in finite element code to investigate deformation problems in the strata and nearby structures caused by the excavation of multi-tunnels. This paper focuses in particular on configurations of two crossing tunnels. Multiple 3D numerical simulations using ABAQUS enable successive analyses conducted for tunnels at different spacings (1.5*D*, 2.5*D*, 3.5*D* and 4.5*D*, where *D* is the tunnel diameter) of configurations aligned vertically. The results, including the ground settlement, lining force and moment, and tunnel convergence, are analyzed. For each aspect, the most unfavorable case is determined by comparing the results of different simulations. This investigation can provide a reference for multi-tunnels design and construction.

Keywords: Multi-tunnels; Anisotropy; Clay; Ground loss; Finite element; Constitutive relation

---

1 Introduction

The rapid development of cities and the continuous population increase require large cities to continuously improve the land utilization rate, creating a growing interest in large cities regarding the development of underground space, followed by the construction of subways, underground passages, urban pipe corridors and so on. However, underground space is limited. To maximize the use of underground space, multi-structure intersections have become increasingly common. In recent years, the development of underground space has been planned in cities such as Beijing, Shanghai and Nanjing (Liao, Peng, & Shen, 2008; Shen & Xu, 2011; Zhang, Liu, Huang, Kwok, & Teng, 2016). However, there are already many existing underground structures, such as pile foundations, municipal pipelines and tunnels, which may hinder the development of three-dimensional underground space use. Therefore, new tunnel construction often needs to bypass existing structures with a parallel or cross configuration (Do, Dias, Oreste, & Djeran-Maigre, 2014; Liu, Li, & Liu, 2011). In addition, the construction of new underground structures affects the normal operation of ground surface structures. Thus, complex crossing tunnels have potential construction risks and safety hazards and

---

* Corresponding author.
E-mail address: zhenyu.yin@polyu.edu.hk (Z.-Y. Yin).

https://doi.org/10.1016/j.undsp.2019.04.002
2467-9674/

adversely affect adjacent structures (e.g., by inducing building cracks or exceeding the bearing capacity of operating tunnels) (Zhang & Huang, 2014). This limitation is especially obvious in soft clay deposits. Therefore, it is necessary to fully understand the land subsidence caused by the construction of crossing tunnels and the impact on existing adjacent tunnels.

It is generally believed that the impact of newly built tunnels on existing tunnels is due to the disturbance of the internal forces of the tunnel structure caused by soil disturbances. At present, there are mainly three methods for studying the multiline crossing of tunnels: (1) empirical or field measurement methods, (2) the model test method, and (3) the numerical analysis method. Based on the field survey data, empirical methods as implemented in a previous study were used to calculate the change of the internal force of the tunnel lining caused by surface settlement and adjacent construction (Harris, Mair, Love, Taylor, & Henderson, 1994; Peck, 1969; Tan & Wei, 2011). It is clear that field observations remain the key to understanding the interaction between adjacent tunnels. Unfortunately, field data are often incomplete. The structural forces induced in tunnel linings are thus hard to obtain. The empirical and analysis method, using the superposition method (Yang & Wang, 2011), is based on the prediction of each tunnel's individual excavation, and the final settlement curve is obtained by superposition. In general, the superposition method cannot rigorously consider the effect of an existing tunnel or the repeated unloading of the ground caused by the previous excavation of the first tunnel; therefore, the settlement curves do not predict the final displacement very well (Divall & Goodey, 2015). Model tests, in particular the centrifuge model test, are another preferred choice for the study of underground works since the same stress state in the tests is used to simulate the actual stress state of the soil (Li, Du, Ma, Yin, & Shen, 2014; Ng, Liu, & Li, 2013). However, the model test study is difficult to implement for large-scale tests. Furthermore, the cost of the model test is high, which limits its application. Recently, the discrete element method was also used to simulate tunnel excavation (Jiang & Yin, 2012, 2014) but only for a small scale with a very limited number of soil particles.

Numerical analysis, as a convenient and effective research tool, has been widely used by researchers and engineers (Jin, Yin, Zhou, & Huang, 2019; Katebi, Rezaei, Hajialilue-Bonab, & Tarifard, 2015; Möller, 2006; Zhang et al., 2016). As far as multi-tunnel excavation is concerned, the introduction of appropriate boundary conditions and appropriate constitutive models (Do et al., 2014) makes it possible to predict land subsidence using numerical analysis methods. Here, the constitutive model of the soil plays an important role. In previous studies, a variety of soil constitutive models were used to analyze problems such as ground settlement caused by tunnel openings, such as nonlinear elastic models with transverse anisotropy (Masın & Herle, 2005), the Mohr–Coulomb model (Shin, Addenbrooke, & Potts, 2002), the modified Cam Clay model (Masın & Herle, 2005), the double surface soil hardening model (Standing et al., 2015) and the hypoplastic model (Masın & Herle, 2005). However, most models are more or less limited in the simulation of the mechanical properties of natural clays; for example, the anisotropy of natural clay is not considered. Therefore, a numerical analysis of the soil model considering the plastic anisotropy could more accurately predict the surface settlement and multi-tunnel interaction in clay.

This paper focuses on the three-dimensional cross-excavation problem of two tunnels. The numerical analysis method is used to study the effect of multi-tunnel excavation on the settlement of the ground surface and the effect on the first tunnel induced by the second tunnel from two aspects: the relative position of the tunnels and the distance between them. A series of three-dimensional finite element models were constructed to consider the intersection of two tunnels with different relative positions and different spacings. In order to consider the influence of soil anisotropy on the excavation problem, the anisotropic elastoplastic constitutive S-CLAY1 was introduced as a user-defined material into the finite element code. Through the above calculations, the analysis of ground settlement caused by the excavation of the crossing tunnels, the change of tunnel internal forces and the convergence of the first tunnel are analyzed and summarized.

2 Numerical models

As described by Divall and Goodey (2015), eight-group plane twin-tunnel centrifuge model tests were conducted to investigate the ground deformation as affected by twin-tunnel excavation. The size of the centrifuge tank is 500 mm × 200 mm × 180 mm, and the radius of the tunnel is 40 mm. The applied acceleration is 100g, where g is the gravitational acceleration. The 2D FEM simulation on investigating the ground deformation affected by twin-tunnel excavation has been validated by comparing simulated results and measured data (Zhu et al., 2018).

In this study, the 2D simulation is extended to 3D simulation for a more comprehensive understanding of the ground deformation affected by multi-tunnel excavation. Thus, a series of three-dimensional finite element simulation models of crossing tunnels is presented. These models take into account the ground volume loss via nonuniform contraction methods. However, only simulated results are presented to show the evolution of volume loss-induced ground deformation because there are no available data under 3D conditions.

2.1 Simulation program

In order to study the soil response caused by the excavation of crossing tunnels and the effects of tunnels on each other, this paper designs a numerical model test for crossing tunnels with 8 different tunnel relative positions and tunnel spacings (see Figs. 1(a) and (b)). In order to reduce the response of the initial state to the first-excavated tunnel caused by tunneling, the location of this first tunnel is fixed. The tunnel diameter $D = 4$ m is determined according to the centrifuge model test under 100*g* (Divall & Goodey, 2015). The lining is assumed to have zero thickness. The tunnel spacing ranges from 1.5*D* to 4.5*D* (both upper and lower sides), where *D* is the tunnel diameter.

2.2 Finite element models

All numerical models in this paper are consistent in size to reduce size effects. In addition, in order to control the boundary effect and reduce the amount of calculation at the same time, according to the recommendations for finite element calculations such as those of Möller (2006), the appropriate boundary conditions are selected based on the distance between tunnels. The largest boundary of the model is determined by the maximum spacing of the tunnel, which is 4.5*D* (case 8) in this study (Fig. 1). The horizontal displacements of the four vertical boundaries of the model sides are fixed, allowing only vertical displacements. The bottom boundary of the model is completely fixed in both the horizontal and vertical directions. The finite element model extends in the depth direction to a minimum depth of four times the tunnel diameter. The width, depth, and length of the final model are all 15*D*, and the model boundaries extend laterally along the tunnel axis to be greater than 5*D* and longitudinally along the tunnel extending beyond 15*D*.

Figure 2 shows the meshed finite element model. Tunnel A is the first tunnel, and tunnel B is the second tunnel. The C3D8R element in ABAQUS is used to simulate the soil in the tunnel excavation (Dong, Burd, Houlsby, & Hou, 2014). The tunnel lining is modeled by an S8R shell element with 4 896 elements per tunnel. The anisotropic elastoplastic constitutive model S-CLAY1 is used to describe the stress-strain relationship of the soil (Wheeler, Näätänen, Karstunen, & Lojander, 2003). The tunnel lining is a segmented structure with bending stiffness, but for the overall response of the tunnel, the discontinuity between the individual concrete elements is negligible, and the lining is modeled as a single tube. The tunnel lining is made of concrete. The common lining material is C55 concrete, which is simulated by a linear elastic model with the parameters $E = 36$ GPa and $\upsilon = 0.2$. In addition, it is assumed that there is no mutual sliding between the tunnel lining and the surrounding soil (see Fig. 3).

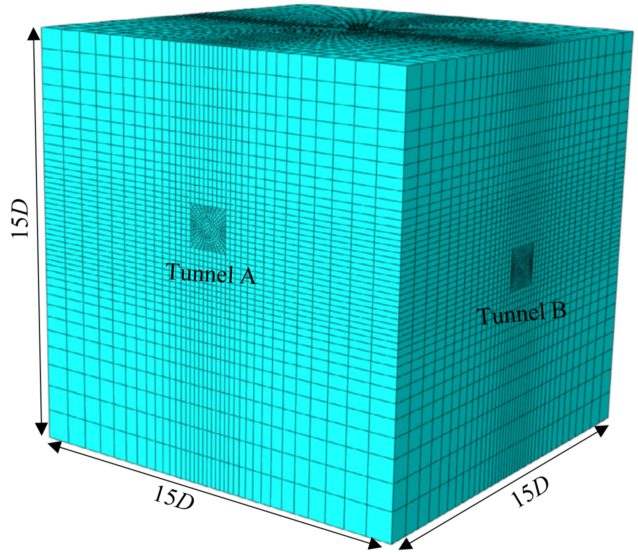

Fig. 2. Meshed finite element model.

2.3 Constitutive model

S-CLAY1 was adopted in this study as an extension of the critical-state-based modified Cam Clay model, with anisotropy of plastic behavior represented through an

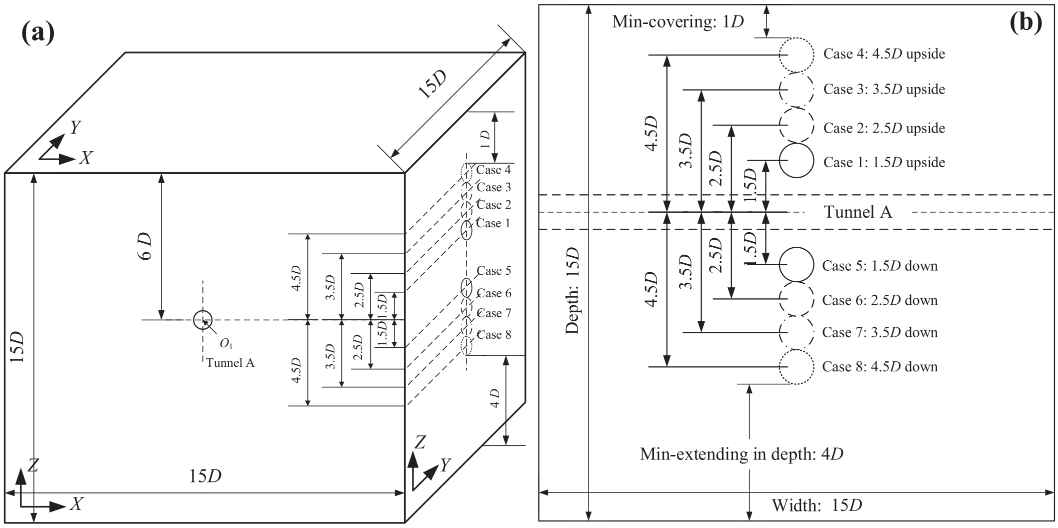

Fig. 1. Cases illustration of the crossing tunnel model: (a) 3D view, and (b) cross-section view.

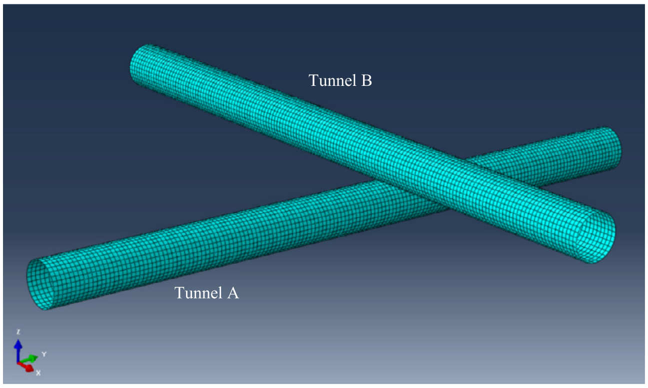

Fig. 3. Meshed model for tunnels.

inclined yield surface and a rotational hardening of the yield surface to describe the development or subsidence of fabric anisotropy during plastic strain. The principle of the model is illustrated in Fig. 4.

The main constitutive equations are summarized as follows:

$$f=\frac{3}{2}\left(s_{ij}-p'\alpha_{\mathrm{d}}\right)\left(s_{ij}-p'\alpha_{\mathrm{d}}\right)+\left(M^2-\frac{3}{2}\alpha_{\mathrm{d}}\alpha_{\mathrm{d}}\right)p'(p'-p_{\mathrm{m}}), \tag{1}$$

$$\delta p_{\mathrm{m}}=p_{\mathrm{m}}\left(\frac{1+e_0}{\lambda-\kappa}\delta\varepsilon_{\mathrm{v}}^{\mathrm{p}}\right), \tag{2}$$

$$\delta\alpha=\omega\left[\left(\frac{3s_{ij}}{4p'}-\alpha_{\mathrm{d}}\right)\left\langle\delta\varepsilon_{\mathrm{v}}^{\mathrm{p}}\right\rangle+\omega_{\mathrm{d}}\left(\frac{s_{ij}}{3p'}-\alpha_d\right)\delta\varepsilon_{\mathrm{d}}^{\mathrm{p}}\right], \tag{3}$$

where f is the yield surface (see Fig. 4), p' is the mean effective stress, q *is* the deviatoric stress, p_{m} is the size of the yield surface, κ is the swelling index, λ is the compression index, e_0 is the initial void ratio, σ'_{ij} is the effective stress tensor, and M is the critical state value of the stress ratio η (where $\eta=q/p'$). $\langle\ldots\rangle$ is Kronecker symbol.

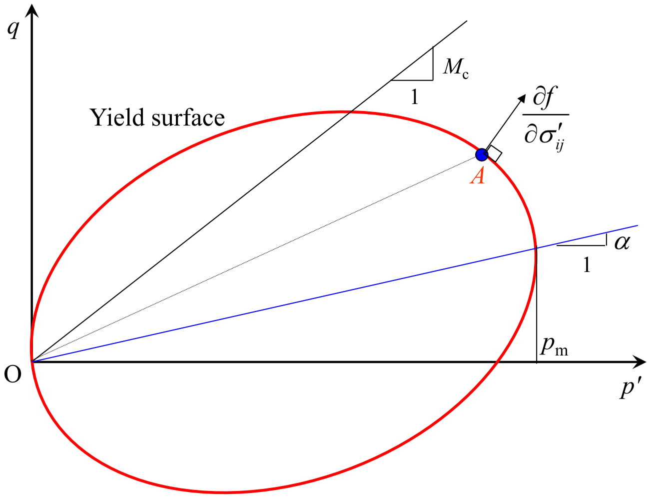

Fig. 4. Yield surfaces of the S-CLAY1 model.

$\alpha=\sqrt{2/3(\alpha_{\mathrm{d}}:\alpha_{\mathrm{d}})}$ is defined with $\alpha_{\mathrm{d}}=\alpha-\delta_{ij}$, and the calculation of Lode angle is modified as $\frac{-\pi}{6}\leqslant\theta=\frac{1}{3}\sin^{-1}\left(\frac{-3\sqrt{3}\bar{J}_3}{2\bar{J}_2^{-3/2}}\right)\leqslant\frac{\pi}{6}$ using $\bar{J}_2=\frac{1}{2}\bar{s}_{ij}:\bar{s}_{ij}$ and $\bar{J}_3=\frac{1}{3}\bar{s}_{ij}\bar{s}_{jk}\bar{s}_{ki}$ with $\bar{s}_{ij}=s_{ij}-p'\alpha_{\mathrm{d}}$.

For the anisotropy of the yield surface, p_{m} and α define the size and inclination of the yield curve, respectively, whereas α is a measure of the degree of plastic anisotropy of the soil. The initial preconsolidation pressure obtained from an oedometer test can be used as an input for calculating the initial size p_{m} from Eq. (1). $\varepsilon_{\mathrm{v}}^{\mathrm{p}}$ and $\varepsilon_{\mathrm{d}}^{\mathrm{p}}$ are the volumetric and deviatoric plastic strains, respectively. The two parameters ω and ω_{d} controlling the rotational hardening of the yield surface can be directly calculated as follows (Wheeler et al., 2003; Yin, Jin, Shen, & Huang, 2017; Yin, Chang, Karstunen, & Hicher, 2010; Yin, Karstunen, Chang, Koskinen, & Lojander, 2011; Yin, Yin, & Huang, 2015):

$$\alpha_0=\alpha_{K_0}=\eta_{K_0}-\frac{M_c^2-\eta_{K_0}^2}{3}\ \text{with}\ \eta_{K_0}=\frac{3M_c}{6-M_c}, \tag{4}$$

$$\omega=\frac{1+e_0}{(\lambda-\kappa)}\ln\frac{10M_c^2-2\alpha_{K_0}\omega_{\mathrm{d}}}{M_c^2-2\alpha_{K_0}\omega_{\mathrm{d}}}\ \text{with}$$
$$\omega_{\mathrm{d}}=\frac{3\left(4M_c^2-4\eta_{K_0}^2-3\eta_{K_0}\right)}{8\left(\eta_{K_0}^2+2\eta_{K_0}-M_c^2\right)}, \tag{5}$$

where α_0 is the initial inclination of yield surface, α_{K_0} is the inclination of yield surface at K_0 state, η_{K_0} is the stress ratio at K_0 state, and M_c is the slope of critical state line in compression condition.

More information about S-CLAY1 can be found in Wheeler et al. (2003). The parameters of S-CLAY1 for the kaolin clay employed in the simulation are summarized in Table 1 according to (Atkinson, Richardson, & Robinson, 1987), who used the same clay. The model with these parameter values was calibrated and validated by simulating centrifuge tests of twin-tunnel excavation under plane strain conditions.

The adopted model was implemented in ABAQUS as a user-defined constitutive model via the user material subroutine UMAT. The procedure of model implementation is similar to that of Wu, Yin, Jin, and Geng (2017), Zhu, Wu, et al. (2014), Zhu, Yin, Wu, and Hicher (2014) and Jin, Wu, Yin, and Shen (2017). For the stress integration, the cutting plane algorithm proposed by Ortiz and Simo (1986) was adopted. According to the flow rule, the plastic

Table 1
Values of model parameters for kaolin clay.

Parameter	υ	e_0	κ	λ	M	POP (kPa)
Value	0.3	1.27	0.035	0.18	0.89	8

Note: POP = $\sigma'_{p0}-\sigma'_{\mathrm{vi}}$, σ'_{p0} is the preconsolidation pressure, and σ'_{vi} is the in situ vertical stress.

multiplier $\mathrm{d}\lambda$ is the key for obtaining the plastic strain. In the cutting plane, $\mathrm{d}\lambda$ is expressed as:

$$\mathrm{d}\lambda=\frac{-f(\boldsymbol{\sigma}_0+\mathrm{d}\boldsymbol{\sigma}_e,\kappa^*)}{-\frac{\partial f}{\partial\boldsymbol{\sigma}}\boldsymbol{D}\frac{\partial g}{\partial\boldsymbol{\sigma}}+\frac{\partial f}{\partial\kappa^*}\frac{\partial\kappa^*}{\partial\boldsymbol{\varepsilon}^p}\frac{\partial g}{\partial\boldsymbol{\sigma}^*}},\tag{6}$$

where κ^* is the hardening parameter (p_m and α_{ij} in the S-CLAY1 model), f is the yield function, g is the potential function (same as f in the S-CLAY1 model and the associated flow rule), $\boldsymbol{\varepsilon}^\mathrm{p}$ is the plastic strain, and $\boldsymbol{D}$ is the elastic matrix.

Figure 5 shows the schematic diagram of a general cutting plane algorithm. The task contains the calculation procedure of the stress increment corresponding to a given strain increment. First, a strain increment $\Delta\boldsymbol{\varepsilon}$ is assumed to be elastic and loaded based on the stress point $\boldsymbol{\sigma}_\mathrm{n}$. Then, the value of the yield function f corresponding to the trial stress point $\bar{\sigma}_{n+1}$ is calculated. If the value of f is smaller than zero, the loading state is inside the elastic domain. Therefore, the stress is updated according to generalized Hooke's law. Otherwise, the loading state is transited from the elastic domain to the elastoplastic domain. The updated stress $\boldsymbol{\sigma}$ and hardening parameter p_m are then calculated using the following equations in the case that both surfaces are activated.

$$\begin{cases}\boldsymbol{\sigma}^{i+1}=\boldsymbol{\sigma}^{i}-\boldsymbol{D}\left(\mathrm{d}\lambda\frac{\partial g}{\partial\boldsymbol{\sigma}}\right)\\ p_\mathrm{m}^{i+1}=p_\mathrm{m}^{i}+\frac{\partial p_\mathrm{c}}{\partial\boldsymbol{\varepsilon}_\mathrm{v}^\mathrm{p}}\left(\mathrm{d}\lambda\frac{\partial g}{\partial p'}\right)\\ \alpha_\mathrm{d}^{i+1}=\alpha_\mathrm{d}^{i}+\omega\left[\left(\frac{3s_{ij}}{4p'}-\alpha_\mathrm{d}^{i}\right)\left\langle\delta\varepsilon_\mathrm{v}^\mathrm{p}\right\rangle+\omega_\mathrm{d}\left(\frac{s_{ij}}{3p'}-\alpha_\mathrm{d}^{i}\right)\delta\varepsilon_\mathrm{d}^\mathrm{p}\right]\end{cases}.\tag{7}$$

The updated terms are then used to update f along the return path shown in Fig. 4 until the loop converges when f is smaller than the tolerance error (e.g., 10^{-7}). The final stress point is obtained as $\boldsymbol{\sigma}_{n+1}$, which is the real stress point corresponding to the strain increment $\Delta\boldsymbol{\varepsilon}$.

Using the implicit integration scheme mentioned above, the trial stress is modified under the consideration of occurring plastic strains as long as convergence is reached. The flow chart of the updating procedure is shown in Fig. 6.

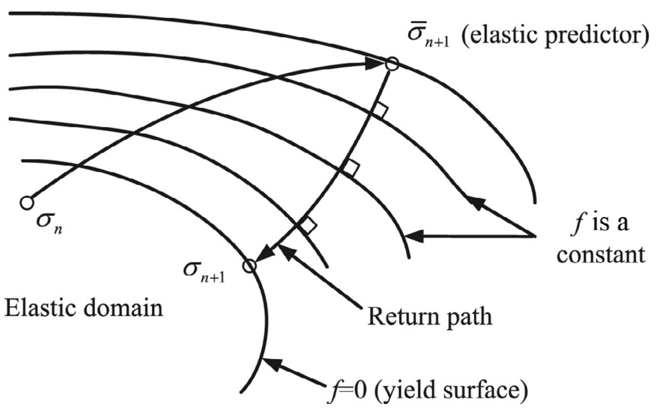

Fig. 5. Schematic diagram of a general cutting plane algorithm.

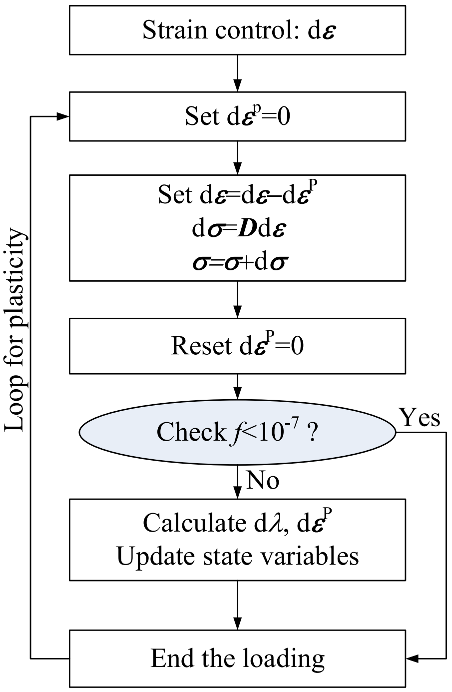

Fig. 6. Flow chart of the cutting plane algorithm.

2.4 Modeling of overexcavation

Excavation is considered to be one of the main causes of the loss of foundation soil. In tunnel shield construction, the difference between the diameter of the cutter head and the shield machine in the shield tunneling process is one of the main reasons for overexcavation. Other factors, such as turning during shield driving, can also lead to overexploitation of foundation soils. In general, the loss of soil caused by overexcavation is strictly controlled by grouting and other methods in the construction of shield tunnels. Considering various factors, the maximum volume loss in this study is 3%, corresponding to a previous model test (Divall & Goodey, 2015).

In the finite element analysis, there are two typical shrinkage models for the modeling of foundation soil loss: uniform shrinkage and nonuniform shrinkage (Lee, Rowe, & Lo, 1992; Sagaseta, 1987). In this study, the nonuniform distribution of the strata loss simulation method was adopted, as shown in Fig. 7. Although this loss model is more complex, it is more consistent with the actual project. In this simulation method, the maximum ground displacement (i.e., δ in Fig. 7) appears at the top of the tunnel, and the "shrinking center" coincides with the center of the tunnel, where Δ is the distance between the excavation center and the center of the tunnel.

The nonuniform contraction mode can then be determined using Eq. (8) according to the geometric relationship shown in Fig. 7:

$$\delta=\frac{\delta_\mathrm{max}}{2(R-R_0)}\left[\sqrt{R^2-2R(R-R_0)\cos(\theta+\pi/2)+(R-R_0)^2}-R_0\right],\tag{8}$$

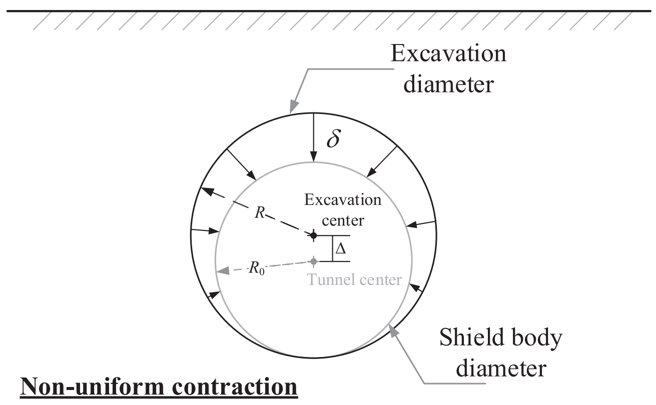

Fig. 7. Nonuniform ground contraction.

where δ is the assumed contraction around the tunnel, $\delta_{\max}$ is the contraction at the tunnel crown, R and R_0 are the radii of the maximum excavation and tunnel, respectively, and θ is the angle of the polar coordinate system with the origin located at the center of the excavation region.

2.5 Modeling of tunnel excavation

The excavation and construction of the tunnel were simulated in a step-by-step procedure, incorporating the “element death” approach, which is widely employed in finite element analysis of excavation problems (Liu, Zhang, & Regueiro, 2014). The whole modeling process is shown in Fig. 8:

(i) In the first phase, the initial stress field is assigned based on the geostatic equilibrium achieved, ensuring that the corresponding deformations are not taken into account in further steps.
(ii) In the second step, the first tunnel (tunnel A) is excavated by deactivating the corresponding excavation volume elements. In addition, the excavation boundary of the over excavated tunnel ring is fixed, shown in Fig. 9 (a).
(iii) Thereafter, nonuniformly distributed displacement boundaries are applied on soil nodes in the perimeter of the excavation space to account for the volume loss, shown in Fig. 9(b).
(iv) The tunnel lining of tunnel A is added. The excavation of tunnel A is completed.
(v), (vi), and (vii) are the steps of excavation for tunnel B, which likely repeats the three steps above.

3 Simulation results

In this study, the ground settlement caused by the excavation of crossing tunnels is studied through calculation and analysis. The axial force, bending moment, tunnel displacement and diameter convergence of tunnel linings are first evaluated.

3.1 Ground settlement

Figure 10 presents the final settlement of the soil after excavation is completed when the 2nd tunnel is constructed above the existing tunnel with different tunnel spacings. As seen from the figure, the settlement of the soil is approximately symmetrical about the tunnel axis, and the maximum vertical displacement occurs near the axis of the tunnel. For the first excavation of tunnel A, the soil at the bottom of the tunnel produces a bulge, which is caused by the unloading of the bottom soil caused by the tunnel excavation. In addition, as the distance between tunnels increases, the settlement of the soil shrinks, and the range of bulging increases.

Figure 11 presents the settlement of tunnel B constructed after tunnel A at different tunnel spacings. Similar to the previous cases, the overall settlement is distributed symmetrically along the axis of the tunnel, and the soil at the bottom of the tunnel is bulging. However, the difference is that as the distance between the tunnels increases, the range of soil uplift in the tunnel decreases, indicating that

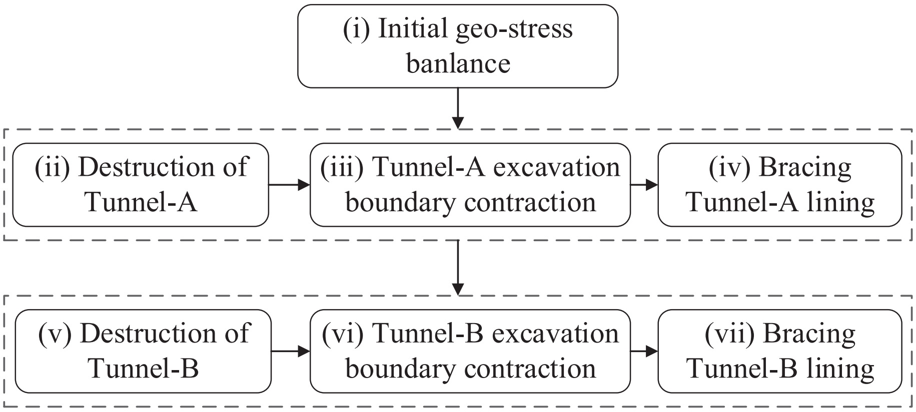

Fig. 8. Numerical simulation steps for tunneling excavation.

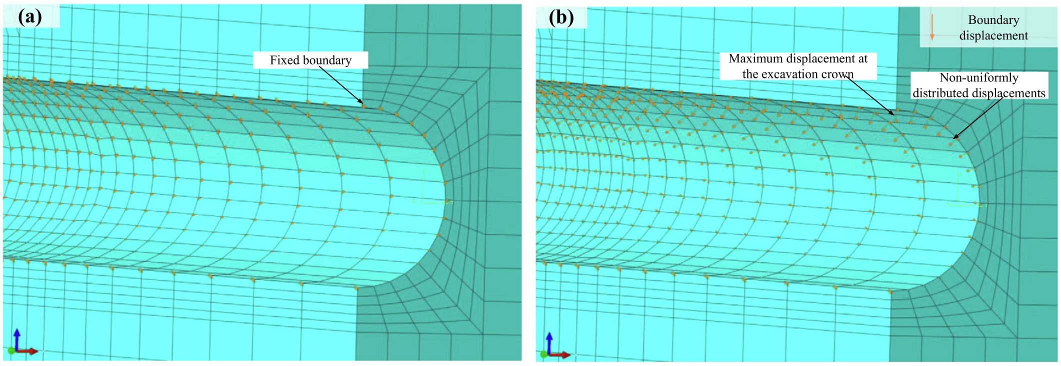

Fig. 9. (a) Local meshed model of the fixed excavation boundary and (b) local mesh model of the nonuniform displacement.

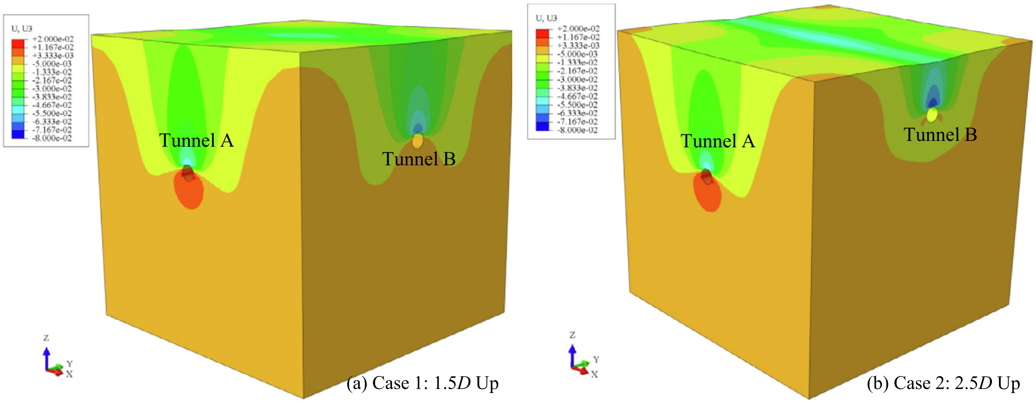

(a) Case 1: 1.5*D* Up (b) Case 2: 2.5*D* Up

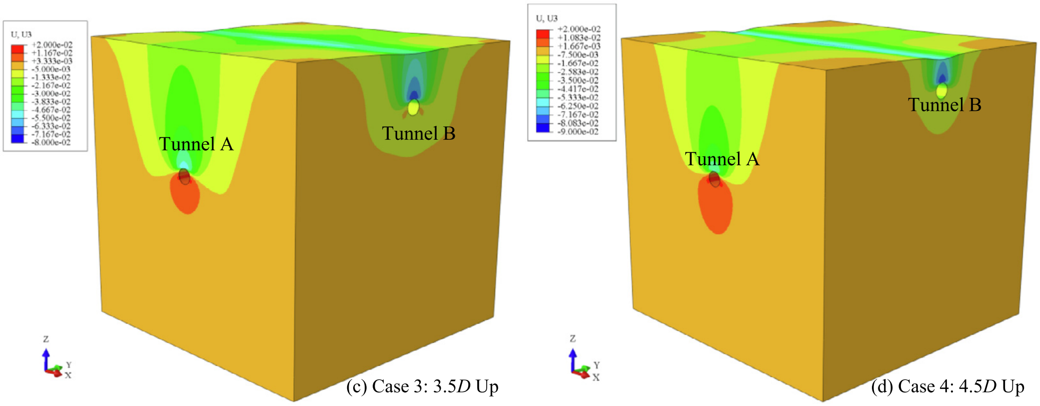

(c) Case 3: 3.5*D* Up (d) Case 4: 4.5*D* Up

Fig. 10. Vertical displacements for the cases where tunnel B is above tunnel A: (a) case 1, (b) case 2, (c) case 3, and (d) case 4.

when the depth of the tunnel is greater, the bulging effect due to stress release decreases.

To further analyze the land subsidence caused by tunnel excavation, cut the section perpendicular to the axis of the tunnel along the longitudinal direction of the two tunnels (see Fig. 12), and plot the surface settlement of the section. The sections taken are divided into two groups according to the section of the tunnel axis, i.e., longitudinal settlement along tunnel A and longitudinal settlement along tunnel B. Six sections are selected in each direction, spaced 1*D* apart, extending outward from the center of the tunnel. The surface subsidence of the section taken will be analyzed and discussed separately in the following sections.

3.2 Ground settlement along the longitudinal direction of tunnel A

Figure 13 shows the final surface settlement along the longitudinal direction of tunnel A when tunnel B passes under tunnel A at different spacings. When tunnel B passes below tunnel A, the surface settlement caused by the change in tunnel spacing changes by a smaller amount.

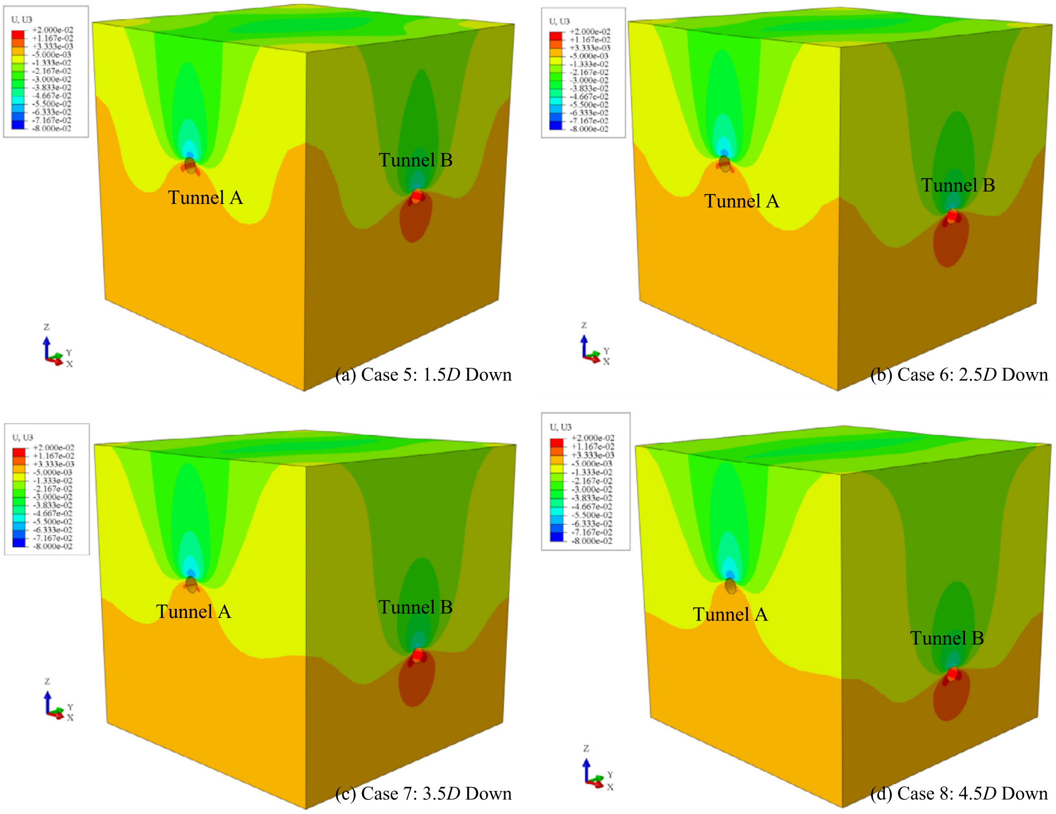

Fig. 11. Vertical displacements for the cases where tunnel B is below tunnel A: (a) case 5, (b) case 6, (c) case 7, and (d) case 8.

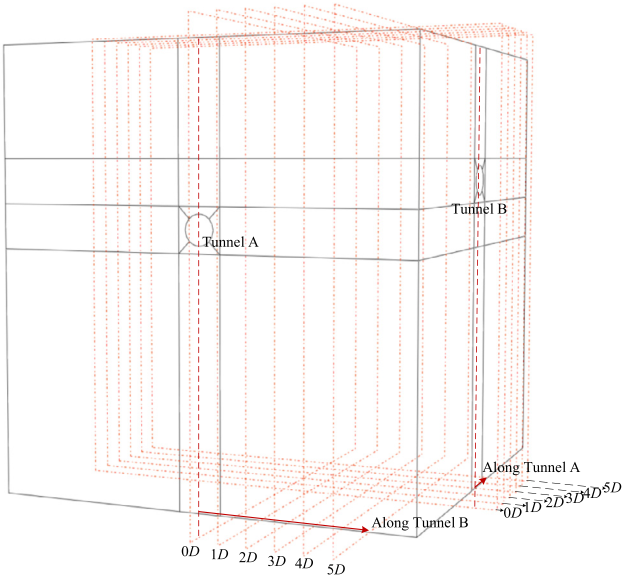

Fig. 12. Vertical sections selected along both tunnels.

Comparing these four cases, the maximum settlement is close to 0.03 m, and the difference in maximum settlement between different cases is very slight. Each case has surface settlement decreasing with increasing distance from the center of the model. The maximum settlement in all cases in which tunnel B passes below tunnel A occurs in the center of the model as well as the center of the tunnel (indicated by the red line in the figure). The blue line in the figure is the 0*D* section settlement curve caused by tunnel A being excavated alone. A comparison of the settlement curves, the red line and blue line, indicates that the maximum settlement after completion of the construction is less than twice the settlement caused by tunnel A excavation.

Figure 14 shows the ground settlement along the longitudinal section of tunnel A when the back-excavated tunnel (tunnel B) is crossed from above. As seen from the figure, the maximum settlement also occurs near the location of the tunnel axis. The maximum settlement at the surface of the tunnel increases with increasing tunnel spacing. The shallower the tunnel is, the more important the ground surface settlement. The maximum settlement is increased from 0.04 m to 0.62 mm when the tunnel spacing increases from 1.5*D* to 4.5*D*. The blue line in the figure is the settlement curve of the 0*D* section when tunnel A is excavated alone, and the red line is the settlement curve of the 0*D* section after completion of the excavation of the two tunnels. Comparing the two curves, it can be seen that the settlement after the final excavation of the tunnels is more than twice as large as that of the excavation of tunnel A. When the tunnel spacing is 4.5*D*, the final settlement exceeds 3 times the settlement caused by excavation of just one tunnel. Similar to the case of the tunnel exposed to operating

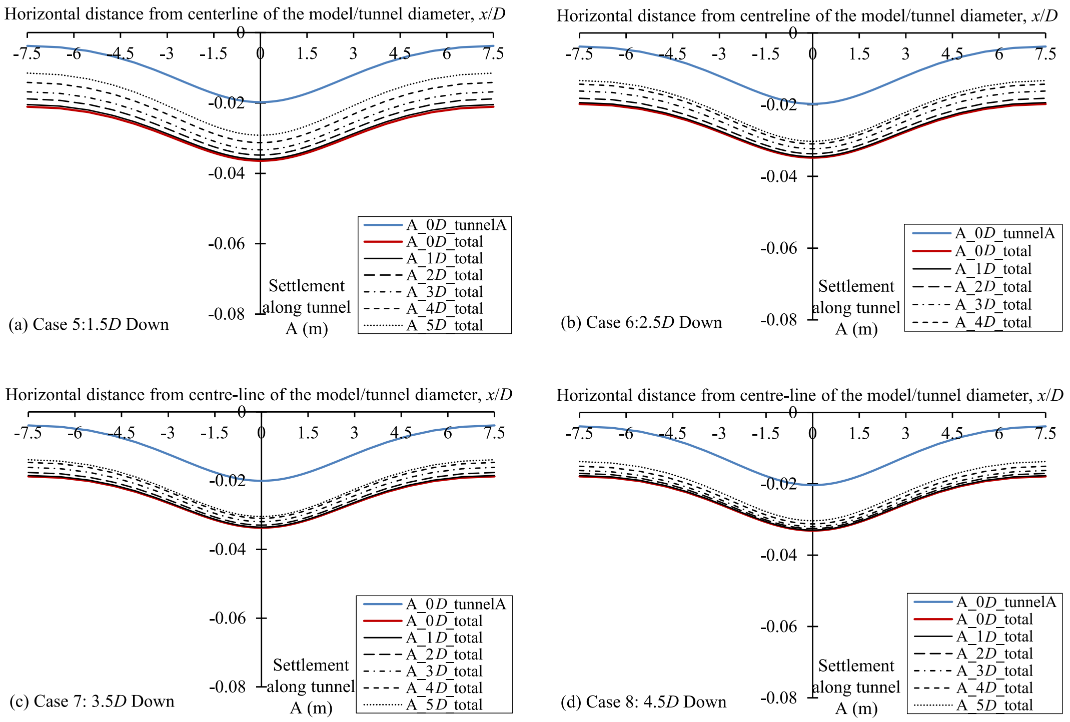

(a) Case 5:1.5*D* Down

(b) Case 6:2.5*D* Down

(c) Case 7: 3.5*D* Down

(d) Case 8: 4.5*D* Down

Fig. 13. Final ground settlements along tunnel A for the cases where tunnel B is below tunnel A: (a) case 5, (b) case 6, (c) case 7, and (d) case 8.

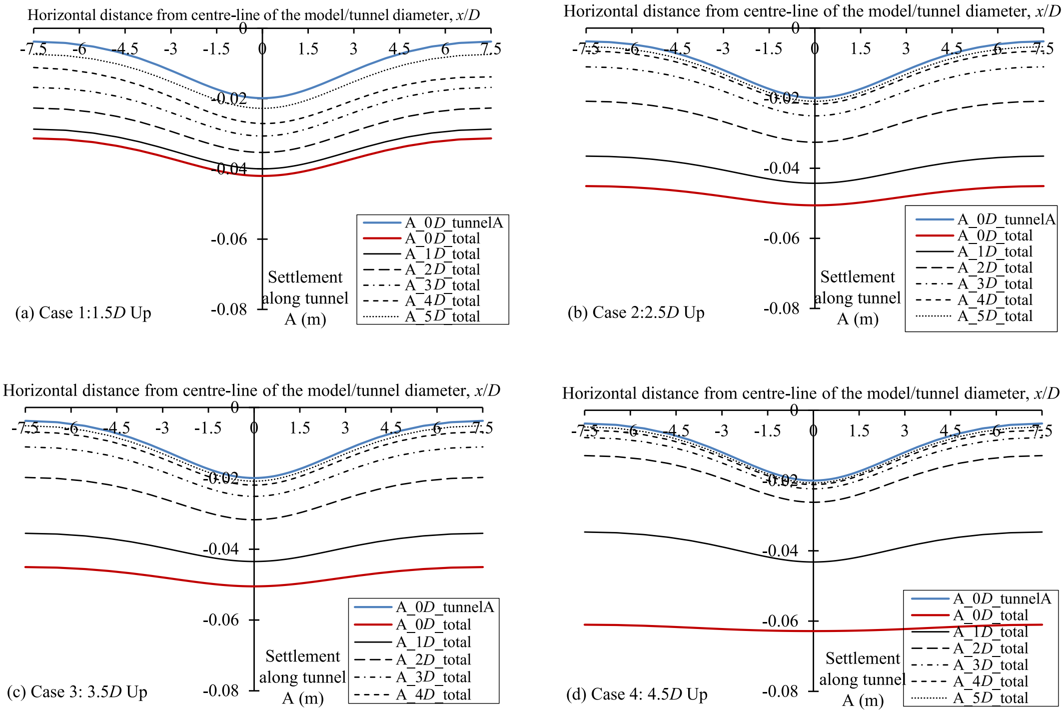

(a) Case 1:1.5*D* Up

(b) Case 2:2.5*D* Up

(c) Case 3: 3.5*D* Up

(d) Case 4: 4.5*D* Up

Fig. 14. Final ground settlements along tunnel A for cases where tunnel B is above tunnel A: (a) case 1, (b) case 2, (c) case 3, and (d) case 4.

conditions, the farther away from the central axis of the tunnel, the shallower the settlement curve is, that is, the smaller the settlement.

Note that the range of the influence zone due to tunnel excavation is significantly affected by the soil model used. In this case, the S-CLAY1 model does not incorporate the small-strain stiffness, so the ground surface settlements at the two ends of the FEM model are too large, and the influence zone of ground surface settlement is too wide. To accurately predict the influence zone of ground surface

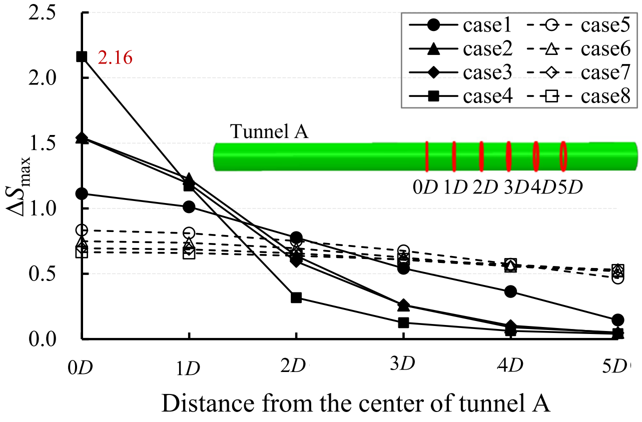

Fig. 15. $\Delta S_{\max}$ along the tunnel A direction in different cases.

settlement, a more advanced soil model considering the small-strain stiffness should be adopted.

To further investigate the ground settlement caused by tunnel excavation of another tunnel, the parameter $\Delta S_{\max}$ was used to study the settlement caused by tunneling. This parameter can be described by Eq. (9). The physical meaning of this value is the ratio of the settlement caused by the excavation of the tunnel after excavation (tunnel B) alone to the settlement caused by the first tunnel (tunnel A).

$$\Delta S_{\max} = \frac{S_{\max,\mathrm{f}} - S_{\max,\mathrm{A}}}{S_{\max,\mathrm{A}}}, \tag{9}$$

where $S_{\max,\mathrm{f}}$ is the maximum settlement of the final settlement of each section and $S_{\max,\mathrm{A}}$ is the maximum tunnel A settlement.

Figure 15 presents a graph of $\Delta S_{\max}$ for different sections. The coordinate is $\Delta S_{\max}$, and the abscissa is the position of the corresponding section. The maximum value of $\Delta S_{\max}$ is greater than that of the condition of crossing below in all the simulation cases when tunnel B is crossing above, while the minimum value of $\Delta S_{\max}$ is less than that of the condition of crossing below. At the same time, for all operating conditions, the settlement gradually decreases as the distance from the crossing center increases. This result shows that the tunnel has an obvious influence on surface settlement when it passes through the existing tunnel, but it has a smaller impact on the surface. The shallower the buried depth of the tunnel, the more pronounced is the change in the $\Delta S_{\max}$ distance at the center of the tunnel. The maximum value of $\Delta S_{\max}$ is 2.16, which occurs in the 4.5*D* condition (in the case where tunnel B is 4.5*D* above tunnel A), indicating that the maximum settlement caused by tunnel B is twice the settlement caused by tunnel A of this case, 1 time more than that of the other cases.

3.3 Ground settlement along the longitudinal direction of tunnel B

This part discusses the longitudinal ground settlement along the tunnel after excavation (tunnel B).

Figure 16 shows the ground subsidence curves of each section along the longitudinal direction of tunnel B when tunnel B crosses below tunnel A. From the figure, it can be seen that the maximum settlement of the surface of each section under different profile floats is in the range of 0.02–

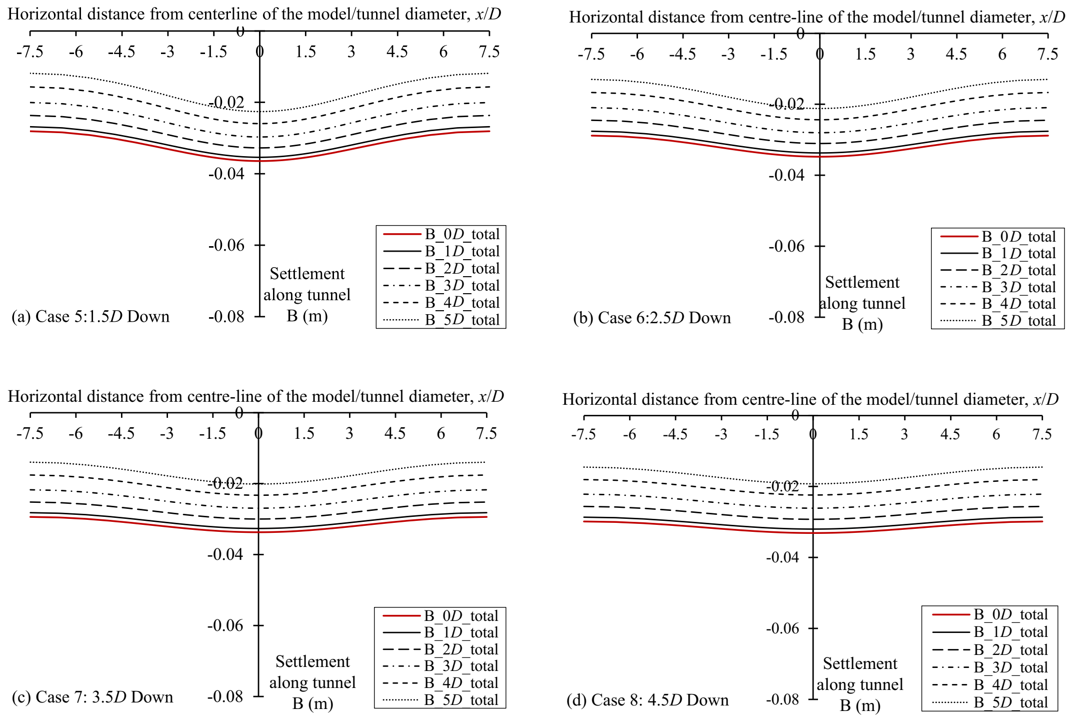

Fig. 16. Final ground settlements along tunnel B for cases where tunnel B passes below tunnel A: (a) case 5, (b) case 6, (c) case 7, and (d) case 8.

0.04 m when tunnel A is crossed from below. As the distance between the profile and the center of the tunnel increases, the surface settlement gradually decreases. When the tunnel subsidence has reached equilibrium, the increase in tunnel spacing has less effect on the maximum settlement. In the four cases shown in Fig. 16, the maximum settlement is approximately 0.036 m.

Figure 17 shows the final settlement curve along the longitudinal direction of tunnel B when tunnel B passes through the region. Under the different conditions of tunneling, the settlement curve changes significantly. The shallower the buried tunnel is (and the larger the tunnel spacing is), the narrower the shape of the settlement tank; in addition, the smaller the extent of propagation from the center is, the larger the maximum settlement. From Figs. 16 and 17, the tunnel has a greater impact on the surface deformation when it traverses from above. In addition, the more the tunnel is buried, the greater the settlement is.

3.4 Axial force of tunnel A affected by excavation of tunnel B

Figures 18 and 19 show the lining axial force after construction. The most severely affected zone for the lining force is near the center of the tunnel (red circle), which is the crossing point in the space projection of the crossing tunnels. When the second tunnel (tunnel B) is above tunnel A, the tunnel A lining axial force distributes more uniformly than the cases in which tunnel B is below tunnel A.

In order to further analyze the influence of tunnel B excavation on the axial force of the tunnel A lining, the axial force of tunnel A after the excavation of the two tunnels was plotted for a typical tunnel section, the tunnel center in the model, where the axial force is most affected (Figs. 20 and 21). It can be seen from the figure that the shape of the axial force of the lining is “peanut-shaped”, and the axial force of the lining is larger at the crown and the bottom and is smaller at the position of the spring line. Figure 20 shows the axial force at the center of tunnel A when tunnel B is above tunnel A. The axial force of tunnel A is most significantly affected when the spacing between the two tunnels is 1.5D. When the spacing between the tunnels is increased to 2.5D, the tunnel A axial force is not greatly changed as a result of tunnel B excavation. This result shows that when a tunnel is crossed from above, the closer the two tunnels are, the greater the influence of the axial force on the tunnel excavation is. In addition, when a tunnel crosses from above, the axial force at the crown of the first tunnel is reduced, and the axial force at the bottom is increased.

Figure 21 shows the axial force diagram of tunnel A during the completion of each excavation step for different cases of tunnel B passing below tunnel A. After tunneling under the existing tunnel, the axial force of tunnel A increases at the crown of the tunnel and decreases at the bottom of the tunnel. Similar to the crossing case described above, the smaller the tunnel spacing is, the greater the influence of the axial force on the tunnel when crossing below. In addition, when the tunnel spacing increases from 1.5D to 4.5D, the axial force of tunnel A is significantly changed due to the excavation of the tunnel underneath. This result shows that the axial force of the lining of an existing tunnel is more significantly affected by the tunneling of an adjacent tunnel below than by tunneling of an adjacent tunnel above.

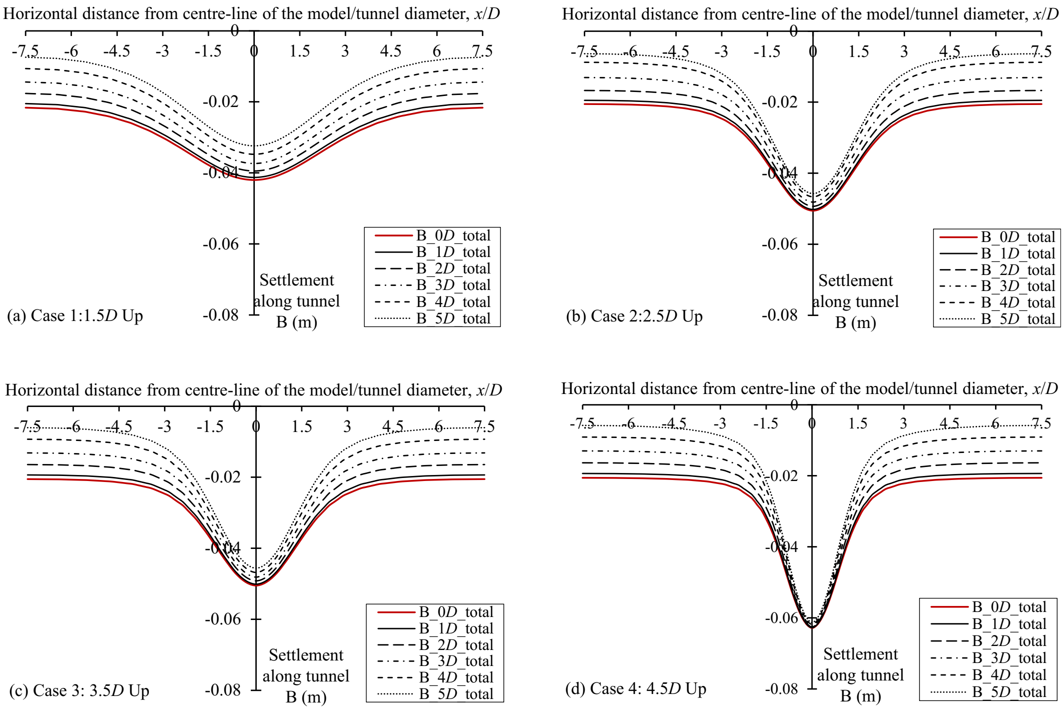

Fig. 17. Final ground settlements along tunnel B for cases where tunnel B is above tunnel A: (a) case 1, (b) case 2, (c) case 3, and (d) case 4.

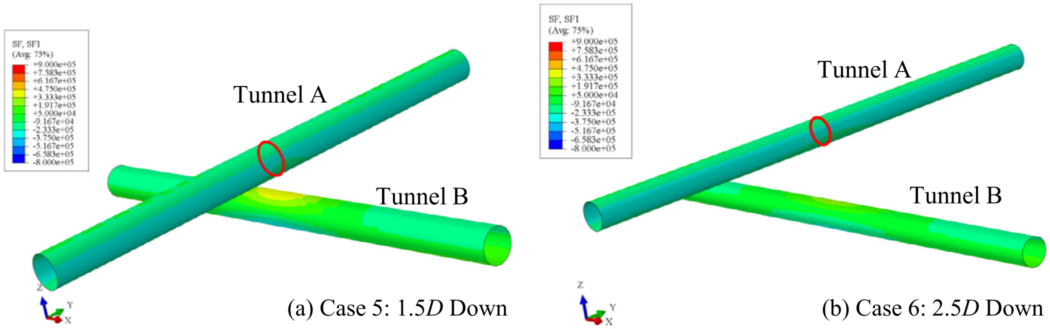

(a) Case 5: 1.5*D* Down

(b) Case 6: 2.5*D* Down

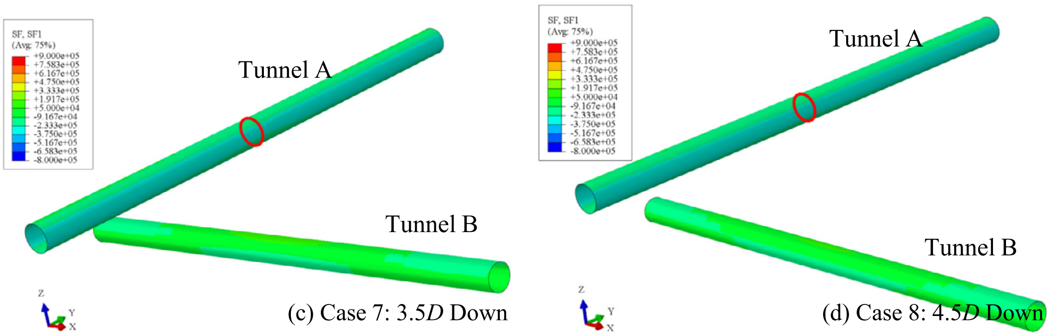

(c) Case 7: 3.5*D* Down

(d) Case 8: 4.5*D* Down

Fig. 18. Final axial lining force for cases where tunnel B is above tunnel A: (a) case 1, (b) case 2, (c) case 3, and (d) case 4.

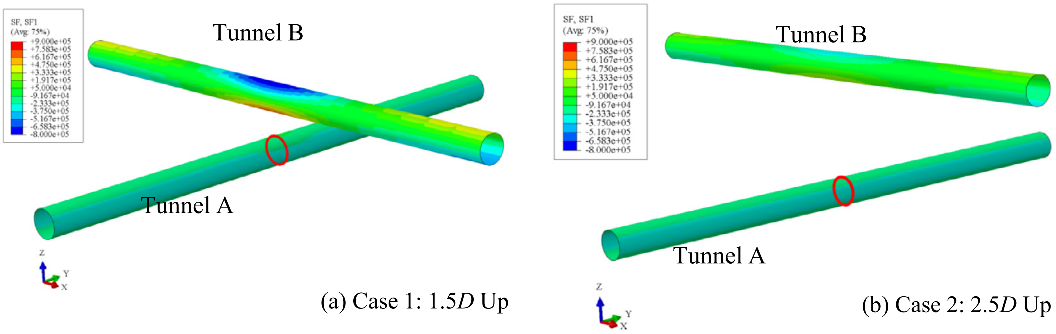

(a) Case 1: 1.5*D* Up

(b) Case 2: 2.5*D* Up

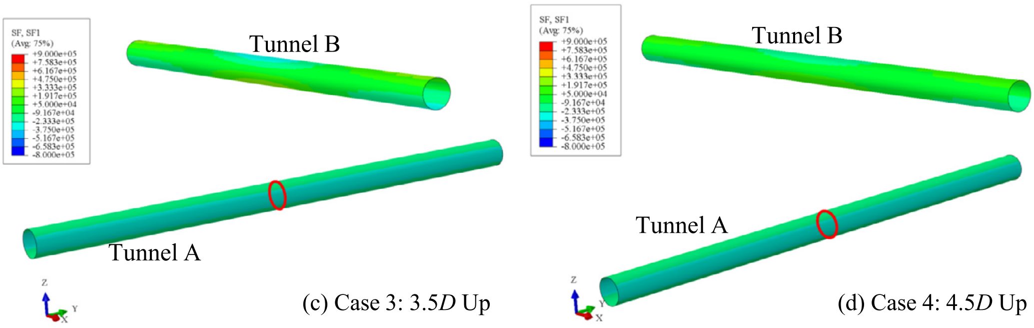

(c) Case 3: 3.5*D* Up

(d) Case 4: 4.5*D* Up

Fig. 19. Final axial lining force for cases where tunnel B is below tunnel A: (a) case 5, (b) case 6, (c) case 7, and (d) case 8.

3.5 Moment of tunnel A affected by the excavation of tunnel B

Figures 22 and 23 show the lining moment of the tunnel lining after excavation. It can be seen from the figures that the area most affected by the lining force is close to the center of the tunnel (red circle), that is, the intersection of the projection of the cross-tunnel space. When the tunnel is crossed from below, the longitudinal distribution of the affected area of the tunnel lining moment center along

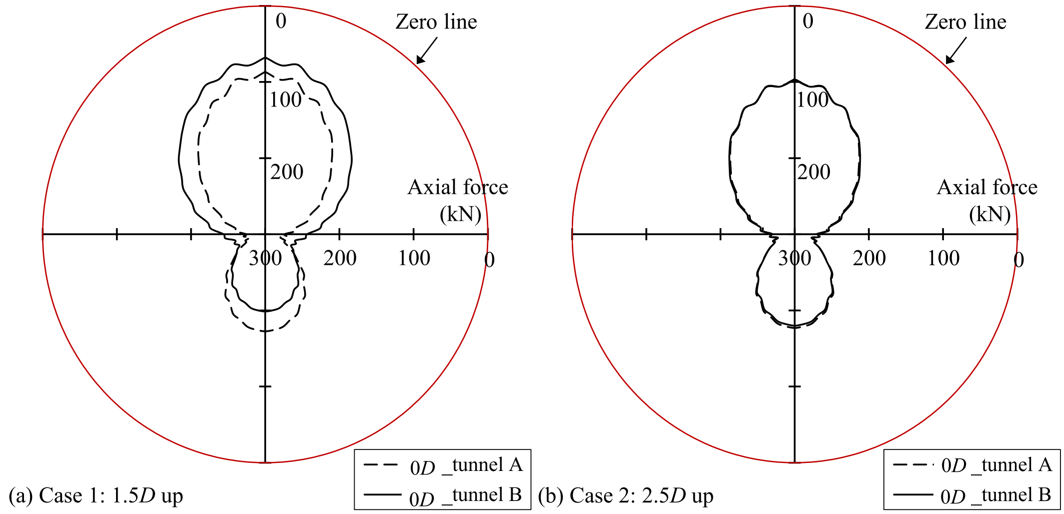

(a) Case 1: 1.5D up (b) Case 2: 2.5D up

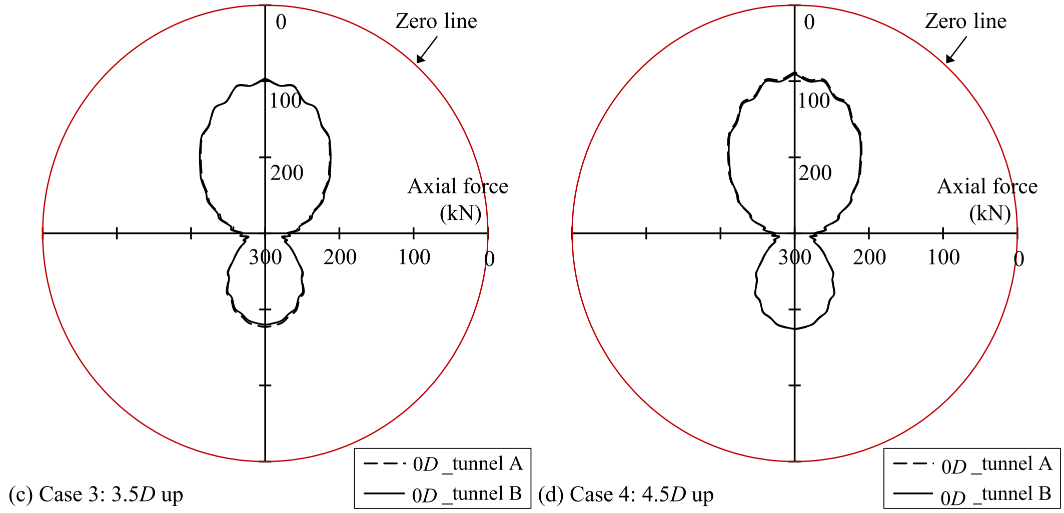

(c) Case 3: 3.5D up (d) Case 4: 4.5D up

Fig. 20. Axial force of tunnel A along the tunnel lining at different stages: (a) case 1, (b) case 2, (c) case 3, and (d) case 4.

the tunnel is greater than that when crossing from above. Similar to the axial force, in order to further analyze the influence of excavation tunnel excavation on the bending moment of the first tunnel lining, the moment at the center of tunnel A, as the typical cross section with the most affected bending moment, appears when tunnel A and tunnel B are excavated separately (Figs. 24 and 25).

Figure 24 shows the lining bending moment of tunnel A during completion of each tunnel excavation when tunnel B is above tunnel A. The moment distribution of the tunnel lining is symmetrically distributed along the tunnel axis. The negative bending moments occur at the tunnel crown and bottom, and the positive moment occurs at the spring line. When the distance between the tunnels is 1.5D, the bending moment of tunnel A changes most obviously during the excavation of tunnel B. With the increase of tunnel spacing, the change of the bending moment in tunnel A caused by the excavation of tunnel B decreases. When the tunnel spacing increases to 2.5D, tunneling near the tunnel has a slight effect on the bending moment of tunnel A. Figure 25 shows the lining bending moment of tunnel A during completion of each tunnel excavation when tunnel B is below tunnel A. The distribution of the bending moment when the tunnel is undercut is the same as that when tunnel B passes above. The smaller the tunnel spacing is, the more obvious is the influence of tunnel excavation on the tunnel A moment. However, different from the case of the second tunnel crossing above the first tunnel, when the distance between the tunnels is increased to 4.5D, the tunnel excavation still has a significant influence on the tunnel A moment. This result shows that the impact on the bending moment of a tunnel being undercut is larger than that of the tunnel underlying a new tunnel.

3.6 Convergence of tunnel A

Tunnel convergence is a widely used parameter to measure the deformation of a tunnel (He, Zhang, & Yang, 2008; Huang & Zhang, 2016). The convergence can be defined as shown in Fig. 26.

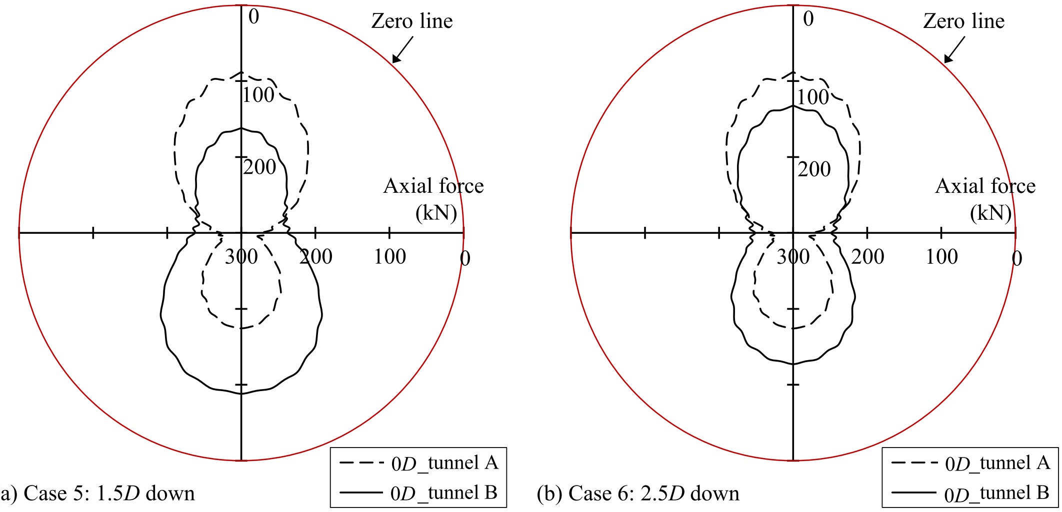

(a) Case 5: 1.5D down

(b) Case 6: 2.5D down

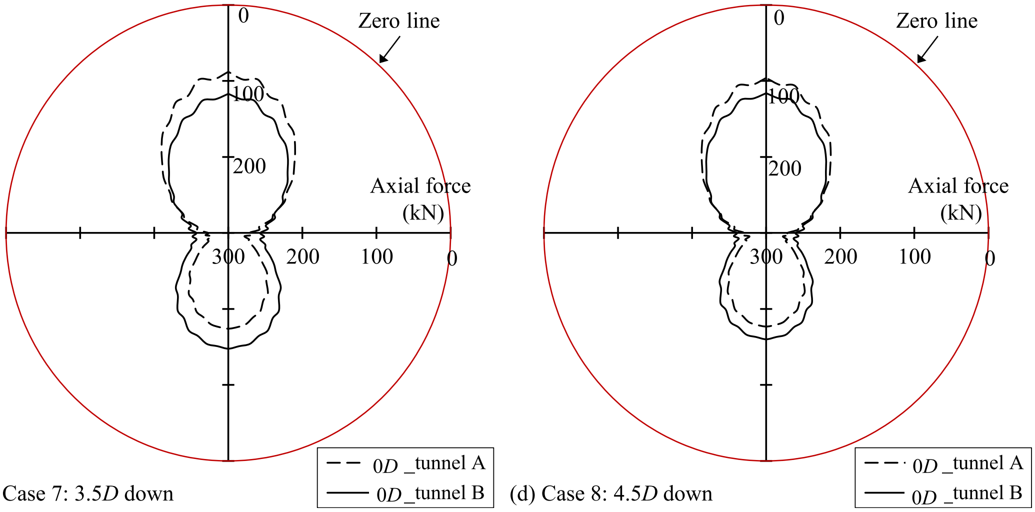

(c) Case 7: 3.5D down

(d) Case 8: 4.5D down

Fig. 21. Axial force of tunnel A along the tunnel lining at different stages: (a) case 5, (b) case 6, (c) case 7, and (d) case 8.

Figure 27 presents some typical sections selected to plot the maximum convergence of tunnel A caused by tunnel B excavation. The maximum convergence of tunnel A is 0.27‰, which occurs in tunnel B passing less than 1.5D under tunnel A (case 5). Tunnel A as affected by tunnel B excavation exhibits greater deformation. When the impact received at the center of the axial force bending tunnel is the largest, for convergence deformation, the convergence occurs at a position deviating from the center of the tunnel. The convergence amount increases from 0D to 3D from the center of the tunnel and decreases when the distance is greater than 3D.

4 Conclusions

This study analyzes the problems caused by tunnel excavation under different three-dimensional intersections of two crossing tunnels with different spacings in a clay foundation. Considering the anisotropy of soft clay, the anisotropic model S-CLAY1 was used to simulate the soil properties in tunnel excavation. Based on model tests and actual engineering conditions, a finite element model of eight crossing tunnels with different tunnel spacings (from 1.5D to 4.5D) was established. Based on numerical simulation results, the ground settlement, lining force, lining torque, and tunnel displacement caused by tunnel excavation under different conditions were analyzed, and the following three conclusions were obtained:

(1) The ground settlement is symmetrical along the axis of the tunnel, and the maximum settlement of the surface is generated at the location of the tunnel axis. The ground settlement caused by the excavation of two crossing tunnels when the second tunnel is excavated above the first tunnel is greater than the settlement when the second tunnel is excavated below the first tunnel. The shallower the buried tunnel is, the larger the maximum settlement on the surface is

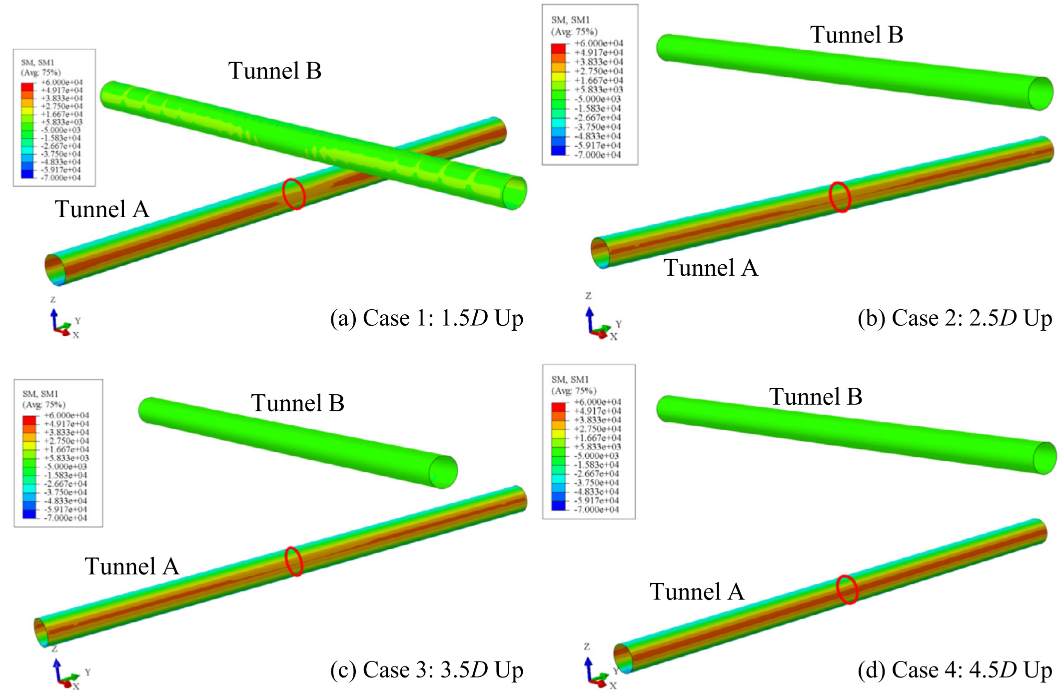

(a) Case 1: 1.5*D* Up

(b) Case 2: 2.5*D* Up

(c) Case 3: 3.5*D* Up

(d) Case 4: 4.5*D* Up

Fig. 22. Final lining moment for cases where tunnel B is above tunnel A: (a) case 1, (b) case 2, (c) case 3, and (d) case 4.

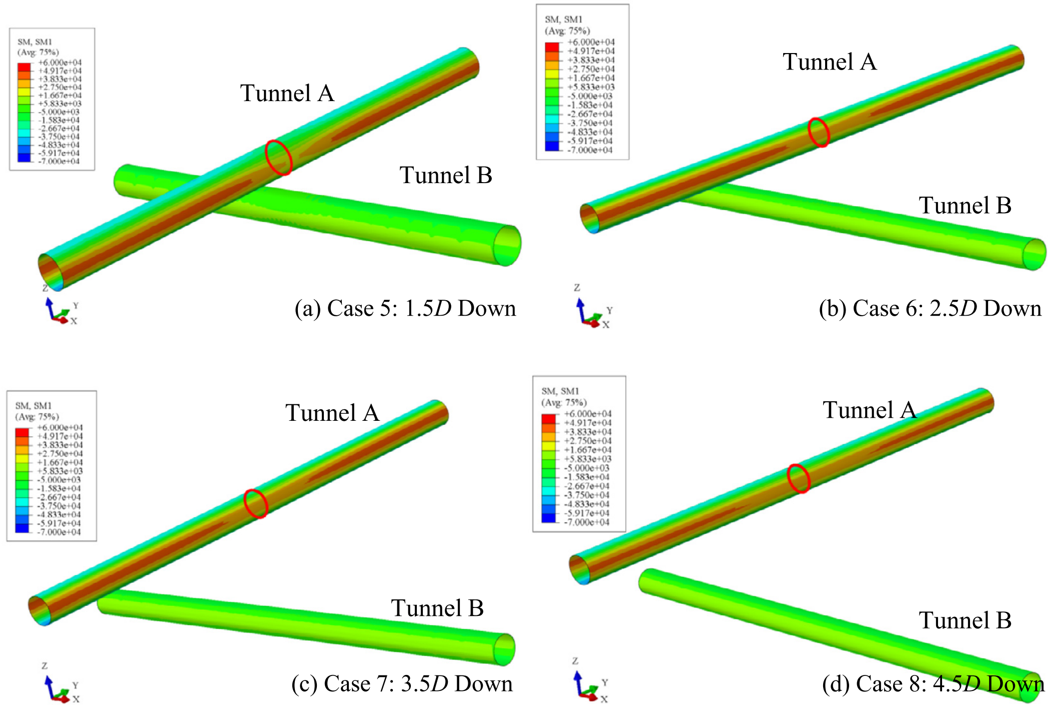

(a) Case 5: 1.5*D* Down

(b) Case 6: 2.5*D* Down

(c) Case 7: 3.5*D* Down

(d) Case 8: 4.5*D* Down

Fig. 23. Final lining moment for cases where tunnel B is below tunnel A: (a) case 5, (b) case 6, (c) case 7, and (d) case 8.

and the narrower the shape of the settlement is. At the same time, the maximum settlement caused by the excavation of crossing tunnels when the second tunnel is excavated above the first tunnel is more than twice that caused by the excavation of the first tunnel. However, the maximum settlement caused by the

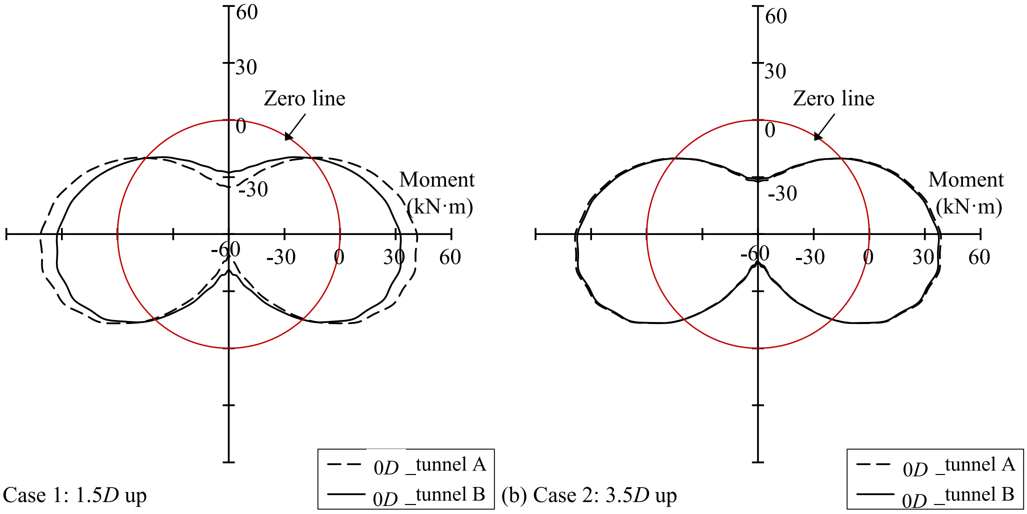

(a) Case 1: 1.5*D* up (b) Case 2: 3.5*D* up

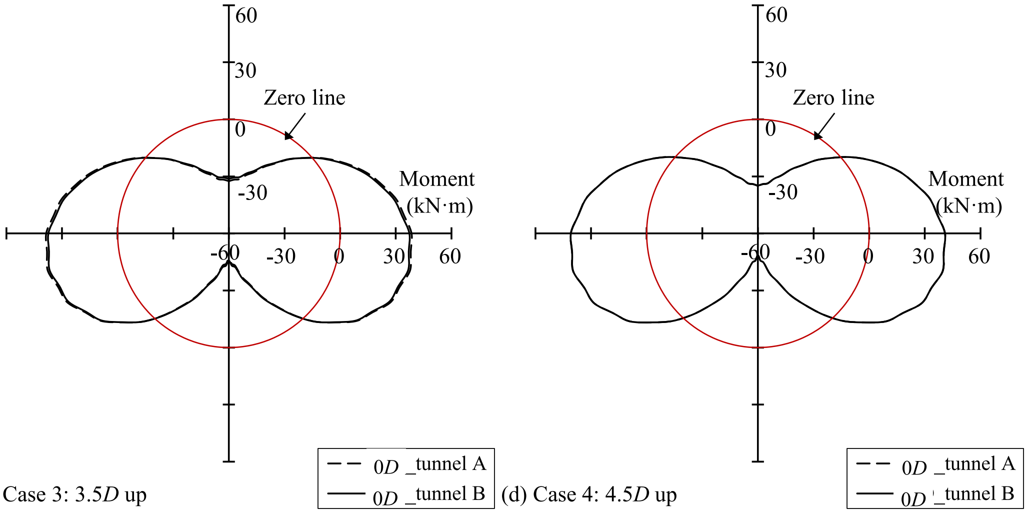

(c) Case 3: 3.5*D* up (d) Case 4: 4.5*D* up

Fig. 24. Moment of tunnel A along the tunnel lining at different stages: (a) case 1, (b) case 2, (c) case 3, and (d) case 4.

excavation of crossing tunnels when the second tunnel is excavated below the first tunnel is less than twice that caused by excavation of the first tunnel.

(2) For the axial force and bending moment of the existing tunnel lining, the most affected area associated with tunnel excavation is located at the crossing point of the tunnels. When the second tunnel is excavated above the first tunnel, the axial force of the existing tunnel lining increases at the crown and decreases at the bottom. The change in the axial force of the lining of the existing tunnel caused by tunnel undercutting is just the opposite, decreasing at the crown and increasing at the bottom. For the axial force and bending moment on the existing tunnel lining, the closer the distance between the tunnels is, the more obvious the influence is on the second tunnel excavation. The change in the axial force and bending moment of the first-excavated tunnel caused by the tunneling is larger when the tunnel is excavated below than when the tunnel is excavated above. When tunneling above, the internal force of the tunnel lining is not significantly affected by the adjacent excavation when the tunnel spacing reaches 2.5*D*. However, even if the tunnel spacing is as large as 4.5*D*, the axial force and bending moment of the first tunnel lining are still evidently influenced when the second tunnel is excavated below. Therefore, for crossing excavated tunnels, undercutting is more likely to have an adverse effect on the internal force of the existing tunnel.

(3) The convergence of the existing tunnel is more significant when the second tunnel passes below than when it passes above. For the convergence of the tunnel deformation, the maximum convergence position does not occur at the intersection of the cross-tunnel space but is offset by a 3*D* distance from the tunnel intersection.

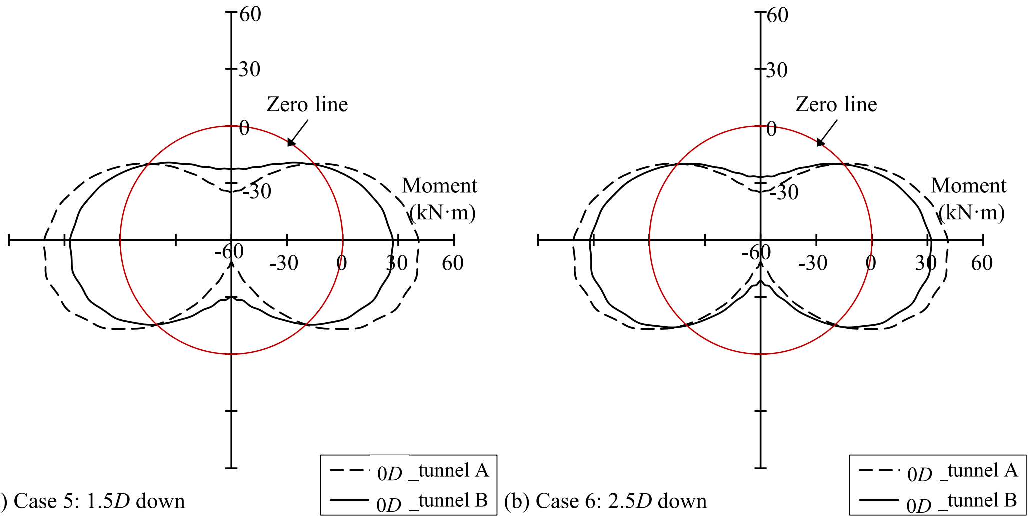

(a) Case 5: 1.5D down

(b) Case 6: 2.5D down

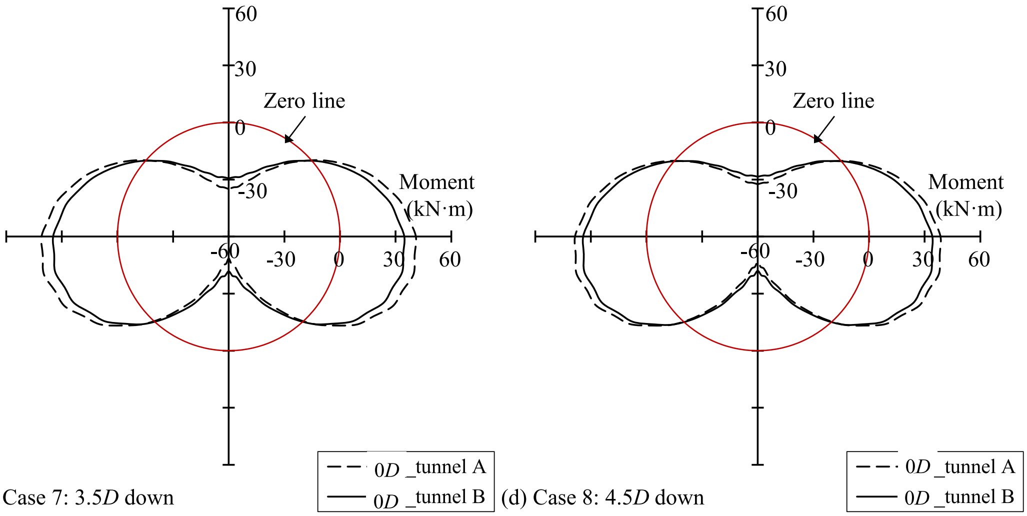

(c) Case 7: 3.5D down

(d) Case 8: 4.5D down

Fig. 25. Moment of tunnel A along the tunnel lining at different stages: (a) case 5, (b) case 6, (c) case 7, and (d) case 8.

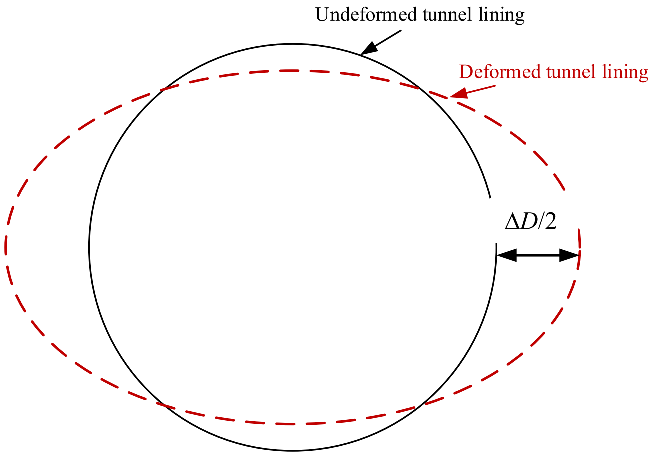

Fig. 26. Definition of the convergence.

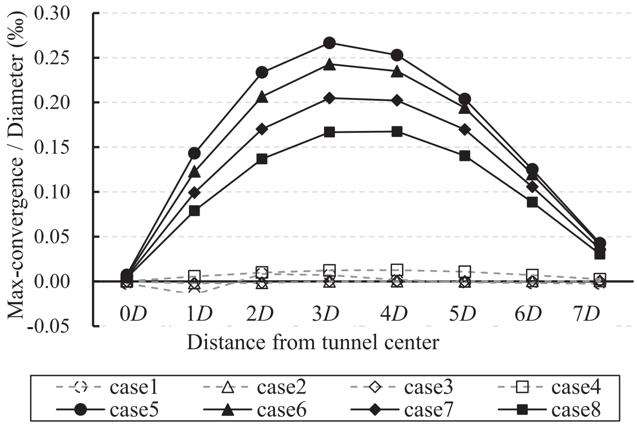

Fig. 27. Convergence/diameter against the distance from the tunnel center.

Acknowledgements

This research project is financially supported by the National Natural Science Foundation of China (No. 51579179).

Declaration of Competing Interest

The authors declare that they have no conflict of interest.

References

Atkinson, J., Richardson, D., & Robinson, P. (1987). Compression and Extension of K0 Normally Consolidated Kaolin Clay. *Journal of geotechnical engineering, 113*(12), 1468–1482.

Divall, S., & Goodey, R. J. (2015). Twin-tunnelling-induced ground movements in clay. *Proceedings of the Institution of Civil Engineers: Geotechnical Engineering, 168*(3), 247–256.

Do, N. A., Dias, D., Oreste, P., & Djeran-Maigre, I. (2014). Three-dimensional numerical simulation of a mechanized twin tunnels in soft ground. *Tunnelling and Underground Space Technology, 42*, 40–51.

Dong, Y., Burd, H., Houlsby, G., & Hou, Y. (2014). Advanced finite element analysis of a complex deep excavation case history in Shanghai. *Frontiers of Structural and Civil Engineering, 8*(1), 93–100.

Harris, D. I., Mair, R. J., Love, J. P., Taylor, R. N., & Henderson, T. O. (1994). Observations of ground and structure movements for compensation grouting during tunnel construction at Waterloo station. *Géotechnique, 44*(4), 691–713.

He, C., Zhang, J. G., & Yang, Z. (2008). Model tests on mechanical characteristics of segment lining structure under multi-layered strata. *Chinese Journal of Geotechnical Engineering, 30*(10), 1537–1543 (in Chinese).

Huang, H. W., & Zhang, D. M. (2016). Resilience analysis of shield tunnel lining under extreme surcharge: Characterization and field application. *Tunnelling and Underground Space Technology, 51*, 301–312.

Jiang, M., & Yin, Z. Y. (2012). Analysis of stress redistribution in soil and earth pressure on tunnel lining using the discrete element method. *Tunnelling and Underground Space Technology, 32*, 251–259.

Jiang, M., & Yin, Z. Y. (2014). Influence of soil conditioning on ground deformation during longitudinal tunneling. *Comptes Rendus Mécanique, 342*(3), 189–197.

Jin, Y. F., Wu, Z. X., Yin, Z. Y., & Shen, J. S. (2017). Estimation of critical state-related formula in advanced constitutive modeling of granular material. *Acta Geotechnica, 12*(6), 1329–1351.

Jin, Y.-F., Yin, Z.-Y., Zhou, W.-H., & Huang, H.-W. (2019). Multi-objective optimization-based updating of predictions during excavation. *Engineering Applications of Artificial Intelligence, 78*, 102–123.

Katebi, H., Rezaei, A. H., Hajialilue-Bonab, M., & Tarifard, A. (2015). Assessment the influence of ground stratification, tunnel and surface buildings specifications on shield tunnel lining loads (by FEM). *Tunnelling and Underground Space Technology, 49*, 67–78.

Lee, K. M., Rowe, R. K., & Lo, K. Y. (1992). Subsidence owing to tunnelling. I. Estimating the gap parameter. *Canadian Geotechnical Journal, 29*(6), 929–940.

Li, P., Du, S. J., Ma, X. F., Yin, Z. Y., & Shen, S. L. (2014). Centrifuge investigation into the effect of new shield tunnelling on an existing underlying large-diameter tunnel. *Tunnelling and Underground Space Technology, 42*, 59–66.

Liao, S. M., Peng, F. L., & Shen, S. L. (2008). Analysis of shearing effect on tunnel induced by load transfer along longitudinal direction. *Journal of Tunnelling and Underground Space Technology, 23*(4), 421–430.

Liu, C., Zhang, Z., & Regueiro, R. A. (2014). Pile and pile group response to tunnelling using a large diameter slurry shield–Case study in Shanghai. *Computers and Geotechnics, 59*, 21–43.

Liu, H., Li, P., & Liu, J. (2011). Numerical investigation of underlying tunnel heave during a new tunnel construction. *Tunnelling and Underground Space Technology, 26*(2), 276–283.

Masın, D., & Herle, I. (2005). Numerical analyses of a tunnel in London clay using different constitutive models. In 5th International symposium TC28 geotechnical aspects of underground construction in soft ground (Vol. 5, pp. 4–2).

Möller, S. C. (2006). *Tunnel induced settlements and structural forces in linings*. Stuttgart, Germany: Univ. Stuttgart, Inst. f. Geotechnik (pp. 108–125).

Ng, C. W. W., Liu, G. B., & Li, Q. (2013). Investigation of the long-term tunnel settlement mechanisms of the first metro line in Shanghai. *Canadian Geotechnical Journal, 50*(6), 674–684.

Ortiz, M., & Simo, J. C. (1986). An analysis of a new class of integration algorithms for elastoplastic constitutive relations. *International Journal for Numerical Methods in Engineering, 23*(3), 353–366.

Peck, R. B. (1969). Deep excavation and tunneling in soft ground. In Proceedings of the 7th international conference on soil mechanics and foundation engineering, Mexico, State of-the-Art Volume (pp. 225–290).

Sagaseta, C. (1987). Analysis of undraind soil deformation due to ground loss. *Géotechnique, 37*(3), 301–320.

Shen, S. L., & Xu, Y. S. (2011). Numerical evaluation of land subsidence induced by groundwater pumping in Shanghai. *Canadian Geotechnical Journal, 48*(9), 1378–1392.

Shin, J. H., Addenbrooke, T. I., & Potts, D. M. (2002). A numerical study of the effect of groundwater movement on long-term tunnel behaviour. *Géotechnique, 52*(6), 391–403.

Standing, J., Potts, D., Vollum, R., Burland, J., Tsiampousi, A., Afshan, S., ... Avgerinos, V. (2015). Investigating the effect of tunnelling on existing tunnels. In *Proceedings underground design and construction tunnelling conference, Hong Kong. IOM3, Hong Kong* (pp. 310–312).

Tan, Y., & Wei, B. (2011). Observed behaviors of a long and deep excavation constructed by cut-and-cover technique in Shanghai soft clay. *Journal of Geotechnical and Geoenvironmental Engineering, 138*(1), 69–88.

Wheeler, S. J., Näätänen, A., Karstunen, M., & Lojander, M. (2003). An anisotropic elastoplastic model for soft clays. *Canadian Geotechnical Journal, 40*(2), 403–418.

Wu, Z. X., Yin, Z. Y., Jin, Y. F., & Geng, X. Y. (2017). A straightforward procedure of parameters determination for sand: A bridge from critical state based constitutive modelling to finite element analysis. *European Journal of Environmental and Civil Engineering*, 1–23.

Yang, X. L., & Wang, J. M. (2011). Ground movement prediction for tunnels using simplified procedure. *Tunnelling and Underground Space Technology, 26*(3), 462–471.

Yin, Z. Y., Chang, C. S., Karstunen, M., & Hicher, P. Y. (2010). An anisotropic elastic–viscoplastic model for soft clays. *International Journal of Solids and Structures, 47*(5), 665–677.

Yin, Z. Y., Jin, Y. F., Shen, S. L., & Huang, H. W. (2017). An efficient optimization method for identifying parameters of soft structured clay by an enhanced genetic algorithm and elastic–viscoplastic model. *Acta Geotechnica, 12*(4), 849–867.

Yin, Z. Y., Karstunen, M., Chang, C. S., Koskinen, M., & Lojander, M. (2011). Modeling time-dependent behavior of soft sensitive clay. *Journal of Geotechnical and Geoenvironmental Engineering, 137*(11), 1103–1113.

Yin, Z. Y., Yin, J. H., & Huang, H. W. (2015). Rate-dependent and long-term yield stress and strength of soft Wenzhou marine clay: Experiments and modeling. *Marine Georesources & Geotechnology, 33*(1), 79–91.

Zhang, Z. X., Liu, C., Huang, X., Kwok, C. Y., & Teng, L. (2016). Three-dimensional finite-element analysis on ground responses during twin-tunnel construction using the URUP method. *Tunnelling and Underground Space Technology, 58*, 133–146.

Zhang, Z., & Huang, M. (2014). Geotechnical influence on existing subway tunnels induced by multiline tunneling in Shanghai soft soil. *Computers and Geotechnics, 56*, 121–132.

Zhu, Q. Y., Wu, Z. X., Li, Y. L., Xu, C. J., Wang, J. H., & Xia, X. H. (2014). A modified creep index and its application to viscoplastic modelling of soft clays. *Journal of Zhejiang University Science A, 15*(4), 272–281.

Zhu, Q. Y., Yin, Z. Y., Wu, Z. X., & Hicher, P. Y. (2014). Uniqueness of time-dependencies for Shanghai soft clay. *Numerical Methods in Geotechnical Engineering, 139*.

Zhu, B.-Q., Jin, Y.-F., Yin, Z.-Y., Zhang, D.-M., & Huang, H.-W. (2018). *Numerical Analysis of Multi-Tunnel Interaction in Clay, GeoShanghai International Conference*. Springer (pp. 412–419). Springer.

Further Reading

Yin, Z. Y., Xu, Q., & Yu, C. (2012). Elastic-viscoplastic modeling for natural soft clays considering nonlinear creep. *International Journal of Geomechanics, 15*(5), A6014001.